International Communications in Heat and Mass Transfer 91 (2018): 165-175. DOI: 10.1016/j.icheatmasstransfer.2017.12.010

NUMERICAL STUDY OF THE MHD FLOW AROUND A BOUNDED HEATING CYLINDER: HEAT TRANSFER AND PRESSURE DROPS

Alessandro Tassone, Matteo Nobili, Gianfranco Caruso

Dep. of Astronautical, Electrical and Energy Engineering, "Sapienza" University of Rome,

Corso Vittorio Emanuele II 244, 00186, Rome, Italy

ABSTRACT

This work studies numerically the flow around an electrically insulated heating cylinder, bounded by walls of non-uniform electrical conductivity and subjected to a transversal magnetic field, with non-null components in the toroidal and poloidal directions. The configuration is representative of a typical breeding blanket segment in tokamak fusion reactors: to minimize magnetohydrodynamic (MHD) pressure drops, the liquid metal can be employed just as tritium breeder, whereas a non-conductive secondary fluid is used as coolant. The coolant is carried in the breeding zone by pipes that, being transversal to the stream-wise direction, affect the flow features and heat transfer. The flow is investigated by simulations performed in a 3D domain for Reynolds number 20 and 40, $0 \leq M \leq 50$ for the Hartmann number and $0° \leq \alpha \leq 32°$ for the magnetic field inclination on the toroidal axis. The transition to the MHD regime causes the suppression of the cylinder wake and the disappearance of the steady vortex structures. Electromagnetic coupling balances the flow rates between the top and bottom sub-channels, individuated by the cylinder. The flow pattern modifications affect the heat transfer, which is found to increase with both M and α in the considered range, albeit for the latter in a non-monotonic trend. The pressure drop in the channel exhibits a similar behaviour. Moreover, the channel pressure drop is dominated by the fully developed component due to the 2D currents, whereas the local one, due to the cylinder presence, decreases steadily with the intensity of the applied magnetic field. The simulations were performed with ANSYS CFX-15.

Keywords: MHD, pressure drop, heat transfer coefficient, flow around cylinder, liquid metals, blanket

International Communications in Heat and Mass Transfer 91 (2018): 165-175. DOI: 10.1016/j.icheatmasstransfer.2017.12.010

Nomenclature

A	Cylinder area [m^2]
B	Magnetic induction (intensity) [T]
c_p	Specific heat capacity [J kg^{-1} K^{-1}]
d	Cylinder diameter [m]
F	Stream-wise length [m]
G	Distance between cylinder bottom and lower wall [m]
H	Poloidal half-length [m]
J	Current density [A m^{-2}]
k	Thermal conductivity [W m^{-1} K^{-1}]
L	Toroidal half-length [m]
p	Pressure [Pa]
r, θ, z	Cylindrical coordinates [m, rad, m]
x, y, z	Cartesian coordinates [m]
T	Temperature [K]
u_0	Inlet mean velocity [m s^{-1}]

Greek symbols

α	Magnetic field inclination [°]
β	Blockage ratio [-]
δ	Thickness [m]
μ	Magnetic permeability [H m^{-1}]
ν	Kinematic viscosity [m^2 s^{-1}]
σ	Electrical conductivity [S m^{-1}]
ϕ	Electric potential [V]

Dimensionless groups

c	Wall conductance ratio
M	Hartmann number
N	Stuart number
Pe	Peclet number
Pr	Prandtl number
Re	Reynolds number

Subscripts

b	Bottom wall, bulk
d	Downstream
H	Hartmann layer
m	Magnetic
s	Side walls
t	Top wall
u	Upstream
w	Wall

1. INTRODUCTION

Magnetohydrodynamic (MHD) flows are employed in a wide range of industrial applications, among which the most important are metallurgy, power generation, materials science, electromagnetic pumps and flow meters [1]. In nuclear fusion applications, a blanket is used to remove the heat deposited by the fusion neutrons, the plasma-facing first wall refrigeration, the breeding of the tritium required for the reactor operation and the radiation shielding for sensible components (i.e. superconducting coils) and personnel. Due to the extreme thermal loads involved in the reactor operation (several MW/m^2), liquid metals (LM) are considered as ideal blanket working fluids due to their excellent thermal properties and the possibility to being used as tritium breeder and neutron multiplier for alloys containing Li [2,3]. However, significant unresolved technological issues are connected to the use of these fluids, one of the most important being the interaction with the plasma confinement magnetic field, which results to the transition to a magnetohydrodynamic (MHD) flow regime.

International Communications in Heat and Mass Transfer 91 (2018): 165-175. DOI: 10.1016/j.icheatmasstransfer.2017.12.010

Typically, the flow of the LM in a fusion blanket can be reduced to a rectangular duct flow in the presence of a strong, transverse, external magnetic field. The fluid motion induces the formation of electric currents which, in turn, interact with the magnetic field to generate Lorentz forces. These exert a retarding action, which can be considered as an additional electromagnetic "drag" term, and modify the flow features, interfering with the heat and mass transport mechanisms [4]. Enhanced corrosion rates of structural materials, turbulence suppression and pressure drops increased by orders of magnitude compared with the hydrodynamic case are among the most important challenges faced by the fusion blanket design [5–9].

To counter this last issue, a common strategy is to minimize the LM velocity, therefore delegating the blanket cooling to a secondary, non-conductive, fluid as water or helium. This solution leads to the necessity to devise a coolant system layout that can efficiently refrigerate the LM that, in this configuration, is considered just as tritium breeder. Most often encountered solutions employ cooling plates or pipes that tailor the LM flow or are immersed in it, both in the stream wise and transverse direction [10–12].

The bounded pressure-driven flow past a circular cylinder is a classic case studied in hydrodynamics and recently it has been investigated in a MHD perspective. The blockage ratio (β) and the offset from the duct centreline (G/d) are the most important geometric parameters and, together with the dimensionless Reynolds number (Re), Hartmann number (M, ratio between electromagnetic and viscous forces) and wall conductance ratio (c, ratio between duct wall and fluid electrical conductivity), define the flow features. The case of a magnetic field transverse to the flow and aligned with the cylinder axis is particularly important for fusion blankets applications and has been studied in the past both experimentally and numerically. The magnetic field is found to retard the transition to unsteady and turbulent regimes, suppress the cylinder wake and, in general, stabilize the flow compared with the hydrodynamic case [13–16].

The aim of this study is to extend the knowledge available for this class of flows by investigating the effect of features that, although commonly encountered in blanket design, have been not sufficiently investigated in the literature such as skewed magnetic field, bounding duct walls of non-uniform thickness and finite conductivity obstacles. The dynamics and heat transfer characteristics of a 3D MHD flow past a confined cylinder in a strong magnetic field were studied for Re = 20 and 40, Hartmann number in the range $0 \leq M \leq 50$ and $0° \leq \alpha \leq 32°$ for the magnetic field inclination on the toroidal axis.

International Communications in Heat and Mass Transfer 91 (2018): 165-175. DOI: 10.1016/j.icheatmasstransfer.2017.12.010

2. FORMULATION

The problem geometry is shown in Fig. 1. A rectangular duct with toroidal half-length L and poloidal half-length H confines a circular cylinder of diameter d. The coordinate system (x, y, z) identifies the radial (streamwise), poloidal and toroidal directions and has its origin in the obstacle centre.

A local cylindrical coordinate system with the same origin (r, θ, z) is also defined, with the z-axis being shared with the global one. The blockage ratio of the obstacle is defined as $\beta = d/2H$. The offset of the cylinder from the duct centreline is obtained from the parameter G/d where G is the distance from the bottom of the cylinder to the nearby wall. The fluid enters the inlet with a constant velocity u_0 in the x-direction. The magnetic field is constant, uniform and transversal to the stream direction with an angle α on the toroidal coordinate axis. The duct walls are assumed as electrically conductive, whereas the cylinder surface is electrically insulated and uniformly heated at a constant wall temperature $T_w = 573$ K. A fixed temperature difference with the fluid at the channel inlet is considered such that $\Delta T = T_w - T_{in} = 30$ K. Finally, the walls are assumed adiabatic and initially at $T_{in} = 543$ K. Main geometrical parameters are available in Table 1.

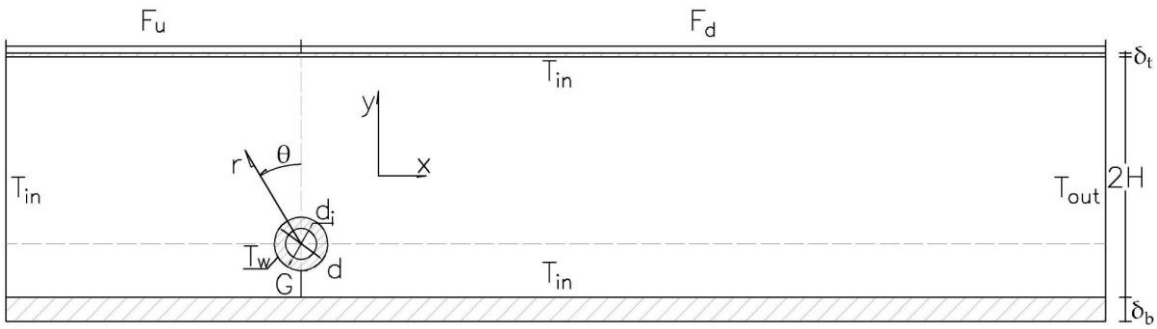

a)

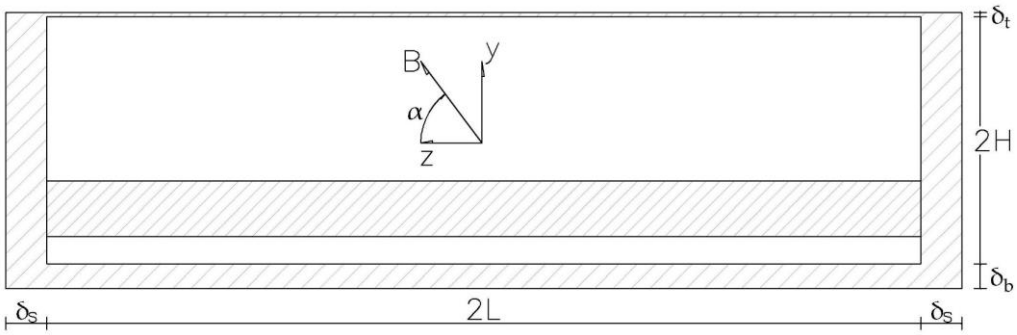

b)

Fig. 1. Test case geometry: a) radial-poloidal cross-section, the inlet is located at the left of the cylinder (x-direction); b) toroidal-poloidal cross-section (view from the inlet)

International Communications in Heat and Mass Transfer 91 (2018): 165-175. DOI: 10.1016/j.icheatmasstransfer.2017.12.010

Table 1

Test case main parameters

Duct [mm]		Cylinder [mm]		Wall thick. [mm]		Conductance ratio $c \times 10^2$	
L	117.00	d	13.500	δ_T	1.00	c_T	1.25
H	30.25	d_i	8.000	δ_B	6.00	c_B	7.50
F_u	74.25	G/d	0.500	δ_S	10.00	c_S	10.00
F_d	202.50	β	0.223	δ_O	2.75	c_O	0

The MHD governing equations are obtained by the combination of the Navier-Stokes' set and the Maxwell's equations. For the parameters usually involved in liquid metal flows, it is possible to simplify the MHD equations employing the induction-less approximation. The influence of the induced magnetic field on the external one is measured by the magnetic Reynolds number Re_m

$$Re_m = \mu\sigma u_0 L \tag{1}$$

where μ and σ are the magnetic permeability and electric conductivity of the fluid. If $Re_m \ll 1$, the magnetic field is determined just by the boundary conditions, i.e. the induced field is neglected [17]. Since this condition is satisfied in the present work, the dimensionless MHD equations for an incompressible, laminar flow can be expressed with the ϕ-(electric potential) formulation as follows [4]

$$\nabla \cdot \mathbf{u} = 0 \tag{2}$$

$$(\mathbf{u} \cdot \nabla)\mathbf{u} + \nabla p - \frac{1}{Re}\nabla^2\mathbf{u} - \frac{M^2}{Re}(\mathbf{J} \times \mathbf{B}) = 0 \tag{3}$$

$$\frac{1}{Pe}\nabla^2 T - (\mathbf{u} \cdot \nabla)T = 0 \tag{4}$$

$$\nabla^2\phi - \nabla \cdot (\mathbf{u} \times \mathbf{B}) = 0 \tag{5}$$

Eqs. (2), (3) and (4) are similar to those employed for an ordinary hydrodynamic flow with the only addition of the source term ${M^2}/{Re}\,(\mathbf{J} \times \mathbf{B})$ to represent the Lorentz force acting on the fluid. A term to represent the power generation due to the Joule effect should be included in (4) but it can be demonstrated how it is negligible for liquid metal flows [15]. Eq. (5) is used to determine the **J** field for a given velocity field at a certain time step through the Ohm's law $\mathbf{J} = \sigma(-\nabla\phi + \mathbf{u} \times \mathbf{B})$. The variables of the equations system (2-5) **u**, p, **B, J** and ϕ are the velocity, pressure, magnetic induction,

current density and electric potential. These variables are scaled by u_0, ρu_0^2, B_0, $\sigma u_0 B_0$ and $L u_0 B_0$ where u_0, B_0, ρ are the inlet velocity, the intensity of the applied magnetic field and the density of the fluid considered. A normalized scaled pressure $\overline{P}$ is defined, assuming $u_0 = 0.345\ \mathrm{mm/s}$, to compare the pressure profiles among cases with different velocities. If not stated otherwise, lengths are scaled by the cylinder diameter d, whereas the dimensionless temperature T is defined as the difference between the local temperature and the inlet temperature T_{in} divided by ΔT.

The dimensionless parameters Reynolds, Prandtl, Peclét, Hartmann and Stuart number are defined as

$$Re = \frac{u_0 d}{\nu} \tag{6}$$

$$Pr = \frac{c_p \rho \nu}{k} \tag{7}$$

$$Pe = Re \cdot Pr \tag{8}$$

$$M = B_0 d \sqrt{\sigma / \rho \nu} \tag{9}$$

$$N = \frac{M^2}{Re} \tag{10}$$

where k, ν and c_p are the thermal conductivity, kinematic viscosity and specific heat capacity of the fluid at constant pressure.

The Hartmann number, Eq. (9), is a measure of the intensity of the applied magnetic field and, therefore, of the flow deviation from the hydrodynamic behavior. It is related to the ratio between the electromagnetic and viscous forces and therefore to the intensity of the magnetic field. Thin boundary layers appear close to the walls perpendicular (Hartmann layers, $\delta_H \propto M^{-1}$) and parallel (Shercliff layers, $\delta_S \propto M^{-1/2}$) to the magnetic field. For $M \gg 1$, the viscous forces are confined to the boundary layers and the flow is inviscid. In the case of skewed magnetic field with $\alpha \gg M^{-1/2}$, the Hartmann layer behavior is observed for each wall with a non-null normal component of the magnetic field [4,18].

Eq. (10) introduces the Stuart number, or interaction parameter, that expresses a balance between the electromagnetic and inertial forces. If $N \gg 1$, the inertia effects are negligible and the flow can be considered laminar and inertia-less. Another dimensionless parameter is needed to describe the influence of the wall conductivity on the flow features, which is called wall conductance ratio

$$c = \frac{\sigma_w}{\sigma} \frac{\delta_w}{L} \tag{11}$$

where σ_w and δ_w are the electrical conductivity and thickness of the wall, respectively. As shown in Fig. 1, the thickness of the walls bounding the flow is non-uniform, therefore the wall conductance ratio for the top (c_t), bottom (c_b) and side (c_s) walls would be different (Table 1). Since the obstacle is assumed as electrically insulating, it is obvious that $c_o = 0$.

The local Nusselt number on the cylinder surface A is defined as

$$\mathrm{Nu_w}(\theta, z) = \frac{d}{T_w - T_b} \frac{\partial T}{\partial r}\bigg|_w \tag{12}$$

where the temperature gradient is evaluated in the direction normal to the surface. The parameter T_b is the bulk fluid temperature that is determined from the velocity and temperature distribution on a cylindrical surface S fixed at a distance $r = d$ from the centre of the obstacle

$$T_b = \frac{\iint_S uT \, d\theta dz}{\iint_S u \, d\theta dz} \tag{13}$$

To quantify the total heat transfer from the obstacle to the wall, an average Nusselt number on A is defined as

$$\mathrm{Nu} = \frac{1}{A} \iint_A \mathrm{Nu_w}(\theta, z) \, dA \tag{14}$$

where $A = 4\pi dL$ is the area of the wetted cylinder surface. The value of the Reynolds number was chosen well below the critical value reported by Frank et al. [13] to focus the analysis on steady-state flow. The increase in the pressure drop compared with the empty duct due to the obstacle presence can be defined as the normalized difference between the calculated drop and the one for the unperturbed channel (Δp_{2D}), calculated considering the fully developed pressure gradient at the channel outlet

$$\Delta p_{2D} = (F_u + F_d) \cdot \frac{\partial p}{\partial x}\bigg|_{\mathrm{outlet}} \tag{15}$$

$$p_O = \frac{\Delta p - \Delta p_{2D}}{\Delta p_{2D}} \tag{16}$$

International Communications in Heat and Mass Transfer 91 (2018): 165-175. DOI: 10.1016/j.icheatmasstransfer.2017.12.010

3. NUMERICAL STRATEGY

3.1 Test case setup

The commercial CFD code ANSYS CFX 15 was used to perform the present study. The MHD model implemented in the code relies on the inductionless approximation [19] and, therefore, solves the equations (2-5) outlined in the previous section. In recent years, this code has been employed to perform many numerical studies of incompressible MHD flows , while being validated against analytical solutions and experimental data for both pressure-driven and natural convection benchmarks [20–23].

The walls bounding the flow have a finite electrical conductivity; therefore Eq. (5) must be solved to determine the electric potential distribution therein. A computational domain composed by a solid (i.e. walls) and a fluid region is established with the electric potential and the normal component of the current density being conserved at the interface. Moreover, a zero-flux boundary condition is imposed for the current density at the solid domain external surfaces, on the cylinder, at channel inlet and outlet.

The RAMS Eurofer 97 steel composes the solid domain, which is a common structural material employed in fusion reactor blanket designs. The lithium-lead eutectic alloy (LiPb) is the fluid selected for the fluid domain. The physical properties of these materials are assumed as constant in the temperature range of the simulation and they are evaluated at a reference temperature $T_{ref} = 558$ K., The correlations from Mergia and Boukos [24] were employed to determine the Eurofer properties, whereas the database realized by Jauch [25] was used for the liquid metal (Table 2). In the adopted conditions, the Prandtl number for the LiPb at the reference temperature is equal to $3.4 \cdot 10^{-2}$.

Table 2

Material properties

	Lithium-Lead [25]	Eurofer97 [24]
ρ [kg m^{-3}]	$9.856 \cdot 10^{3}$	$7.695 \cdot 10^{3}$
σ [S m^{-1}]	$7.932 \cdot 10^{5}$	$1.259 \cdot 10^{6}$
κ [W m^{-1}K^{-1}]	12.831	30.060
ν [m^{2}s^{-1}]	$2.332 \cdot 10^{-7}$	-
α_t [m^{2}s^{-1}]	$6.885 \cdot 10^{-6}$	$7.193 \cdot 10^{-6}$

Typical velocities in the breeding zone for separate cooling fusion blanket ranges from 0.1 mm/s to 5 mm/s and this, accounting for the stabilizing effect of the magnetic field, ensures the maintenance of a steady and laminar regime [5,11]. The simulations conducted focused on low Re, steady-state,

flow ($\mathrm{Re} = 20$ and $\mathrm{Re} = 40$) with inlet velocity in the range $0.345\ \mathrm{mm\ s^{-1}} \leq \mathrm{u_0} \leq 1.38\ \mathrm{mm\ s^{-1}}$. Therefore, from Eq. (8), Péclet number is $0.68 \leq \mathrm{Pe} \leq 2.72$. A uniform velocity profile was assumed at the inlet, whereas at the outlet a zero pressure was specified. The calculated magnetic Reynolds number is $O(10^{-6})$, which widely satisfies the condition for the induction-less approximation employed by the code.

For an operative fusion blanket, the magnetic induction intensity leads to $\mathrm{M} = O(10^3)$. Since no computational MHD code available can perform 3D calculations for this value [26], the Hartmann number considered for the study was $10 \leq \mathrm{M} \leq 50$. For any M value, an angle $\alpha = 16°$ of the magnetic field on the toroidal coordinate axis was considered. Since the poloidal component can change up to $\pm 50\%$ during the blanket operation, additional simulations were performed for $\mathrm{M} = 10$ to assess the influence of the magnetic field orientation on heat transfer and pressure drops [27]. Calculations for purely toroidal magnetic field ($\alpha = 0°$) and hydrodynamic flow were performed to provide reference cases. Only steady-state cases were considered. A full overview of the test matrix is available in Table 3.

Table 3

Test matrix parameters

M	Re	Pe	N	α (°)
10	20	0.68	5	0, 8, 16, 24, 32
	40	1.36	2.5	0, 8, 16, 24, 32
30	20	0.68	45	16
	40	1.36	22.5	16
50	20	0.68	125	16
	40	1.36	62.5	16

All the simulations were performed with the “high resolution” advection scheme that is a local-weighted version of the upwind discretization scheme. CFX employs a coupled solver, which calculates simultaneously Eqs. (2-5). The steady-state algorithm uses a virtual time step to under-relax the equations and improve numerical stability. For the analysis, the Local Timescale option was selected for the calculation of the time step, which enables the code to weigh the value with the local velocity field. The value calculated is then adjusted by the application of a reduction factor [28]. A factor between 0.5 and 4 was enough to achieve reasonable convergence speed for all the simulations.

International Communications in Heat and Mass Transfer 91 (2018): 165-175. DOI: 10.1016/j.icheatmasstransfer.2017.12.010

3.2 Domain discretization

This class of problems is usually modelled employing the quasi-2D approximation developed by Sommeria and Moreau [29], e.g [15,30], etc. In this study, a full 3D computational domain was required due to the complex magnetic field topology and non-uniform wall conductivity. A critical aspect for the mesh of a MHD flow is to provide enough nodes (~10) in the thin boundary layers. This condition is necessary to follow the steep velocity gradient present therein and can lead to excessive computational costs for high M values. A conformal mesh for the solid and fluid domain is required to calculate the electric potential distribution in the walls. If this condition is not met, numerical errors are introduced due to the imperfect coupling between the domains. An example of the non-uniform mesh employed is available in Fig. 2.

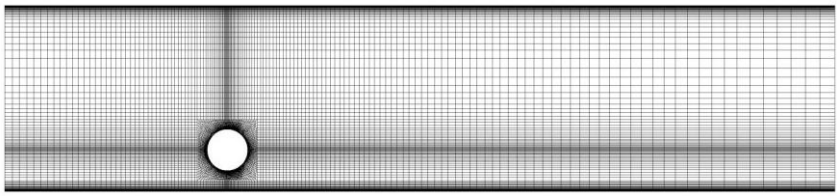

a)

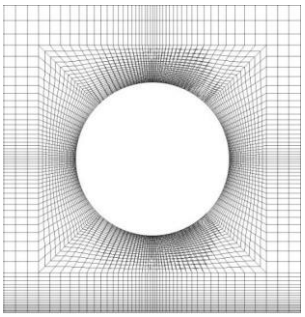

b)

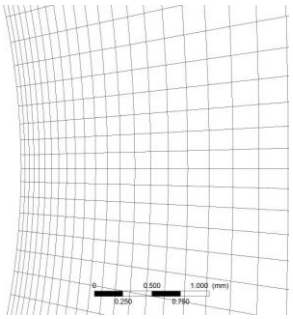

c)

Fig. 2. a) Example of the mesh employed in the study, b) detail of the grid refinement around the obstacle, c) Hartmann layer resolution close to the cylinder surface (i.e. $\delta_H \sim 1.35$ mm)

3.3 Mesh sensitivity

A study was carried over to ensure the independence of the results obtained from the grid resolution. Five mesh with increasing refinement (number of nodes) on the cylinder circumference ($N_\emptyset$), the upstream (N_U) and downstream (N_D) direction (Table 4) were considered for flow with $\mathrm{Re} = 20$ and $\mathrm{M} = 10$. The dimensionless parameters monitored were the average temperature of the fluid at the outlet (T_{out}), the average Nusselt number on the cylinder surface (Nu) and the pressure drop in the

channel (Δp). An error of less than 2% compared with the result of the most refined mesh (Grd_5) was found for all the parameters (see Table 4). The mesh Grd_3 was chosen as the reference for the study and was employed for all the simulations, slightly changing the element grading toward the wall to account for the shrinking of the Hartmann layer.

Table 4

Mesh sensitivity results

	Grd_1	Grd_2	Grd_3	Grd_4	Grd_5
$N_{\emptyset}$	100	120	160	200	240
N_U	24	29	39	49	59
N_D	48	58	77	97	115
N° cells	$4.56 \cdot 10^5$	$6.79 \cdot 10^5$	$1.42 \cdot 10^6$	$2.49 \cdot 10^6$	$3.96 \cdot 10^6$
T_{out}	0.682	0.669	0.675	0.679	0.678
Nu	2.585	2.551	2.567	2.572	2.571
Δp	76.628	76.605	76.580	76.574	76.575

4. RESULTS AND DISCUSSION

4.1 *Fluid flow field and pressure drop*

The flow velocities considered are low enough that the flow maintains the laminar and steady state throughout the analysis. This circumstance is desired, since the LiPb is not expected to make the transition to the turbulent regime in separate cooling blanket design [12,10].

Simulations were performed with no magnetic field applied to provide reference for the MHD results. At $Re = 20$, the flow around the cylinder is almost symmetric with a perfect wetting of the heated surface and indistinct wake (Fig. 3). The proximity with the duct bottom wall reduces the cross-section available for the flow in the sub-channel below the cylinder, which carries only 6% of the total mass flow rate. For $Re = 40$, a more consistent wake develops with the appearance of steady vortex structures. However, the wake is far from symmetric due to the wall effect and the high velocities in the sub-channel above the cylinder. The main flow stretches the top vortex, whereas the bottom one retains its original structure. The obstacle has a significant effect on the pressure drop in the cross-section, as reported in Table 5, with an increase between the 193% and 451% compared with the unperturbed flow.

International Communications in Heat and Mass Transfer 91 (2018): 165-175. DOI: 10.1016/j.icheatmasstransfer.2017.12.010

Table 5

Pressure drop and flow rate distribution in the channel

M	0		10		30		50	
Re	20	40	20	40	20	40	20	40
Δp $(Pa\cdot 10^3)$	2.28	6.28	9.66	18.95	94.90	187.28	269.61	498.30
$d\overline{P}/dx^{\dagger}$	0.032	0.048	0.339	0.540	3.505	6.956	10.165	18.277
Δp_{3D} (%)	193[§]	451[§]	18.38	45.84	12.26	11.63	10.28	13.36
$\dot{m}$ (%) $y > 0$	94.0	90.8	90.6	88.5	73.7	78.25	71.8	70.4
$\dot{m}$ (%) $y < 0$	6.0	9.2	9.4	11.5	26.3	21.85	28.2	29.6

[§]Unperturbed pressure drop in the channel compared with flow far from the cylinder

[†]Normalized pressure gradient $(-dp/dx)\cdot d/(\rho u_0^2)$, where $u_0 = 0.345$ mm s^{-1}

In Fig. 4, the transition of the flow from the hydrodynamic to the MHD regime is presented. In the former, the fully developed flow downstream the cylinder assumes the typical parabolic Poiseuille profile for every radial-poloidal plane. This is no longer the case for the MHD flow where, even for $M = 10$, the boundary layers shrink noticeably assuming the thickness $\delta_H \propto 1/M$, characteristic of the Hartmann layers [4]. The Hartmann layer behaviour dominates in the test section since the magnetic field has a non-null normal component for every wall. For a purely toroidal magnetic field, boundary layers of thickness $O(M^{-1/2})$ would appear alongside the top and bottom wall, which would be aligned with the magnetic field [31]. These are called *Shercliff layers* and, for $c \neq 0$ walls, are characterized by jets. Since $\alpha > M^{-1/2}$, the boundary layer detaches from the wall and the jet is smeared over the core region creating an internal layer that follows the magnetic field lines and connects two opposite duct corners. A free shear layer of thickness $O(M^{-1/2})$ is observed perpendicular to the field direction, which bridges the gap between the Hartmann layer and the internal one. Moreover, the top wall, which has relatively low conductivity compared with the bottom one, promotes the flow in the surrounding area, whereas the opposite effect is observed close to the thicker, thus more conductive, bottom wall.

Downstream from the obstacle, the magnetic field restores more quickly the fully developed state compared with the hydrodynamic case. At $M = 10$ and $Re = 40$, the wake vortices which were stretched by the flow in the $M = 0$ simulation are regularized and the top structure retains its symmetry to the bottom one (see Fig. 3). However, the wake length is shortened with the separation points moving downstream. This trend is confirmed with increasing M. At $M = 50$, the wake is

International Communications in Heat and Mass Transfer 91 (2018): 165-175. DOI: 10.1016/j.icheatmasstransfer.2017.12.010

completely suppressed and the fluid wets uniformly the cylinder surface for any value of Re considered (Fig. 3). The front stagnation point shows a similar behaviour, being gradually shifted toward the top of the cylinder due to the increase of the flow rate in the bottom sub-channel.

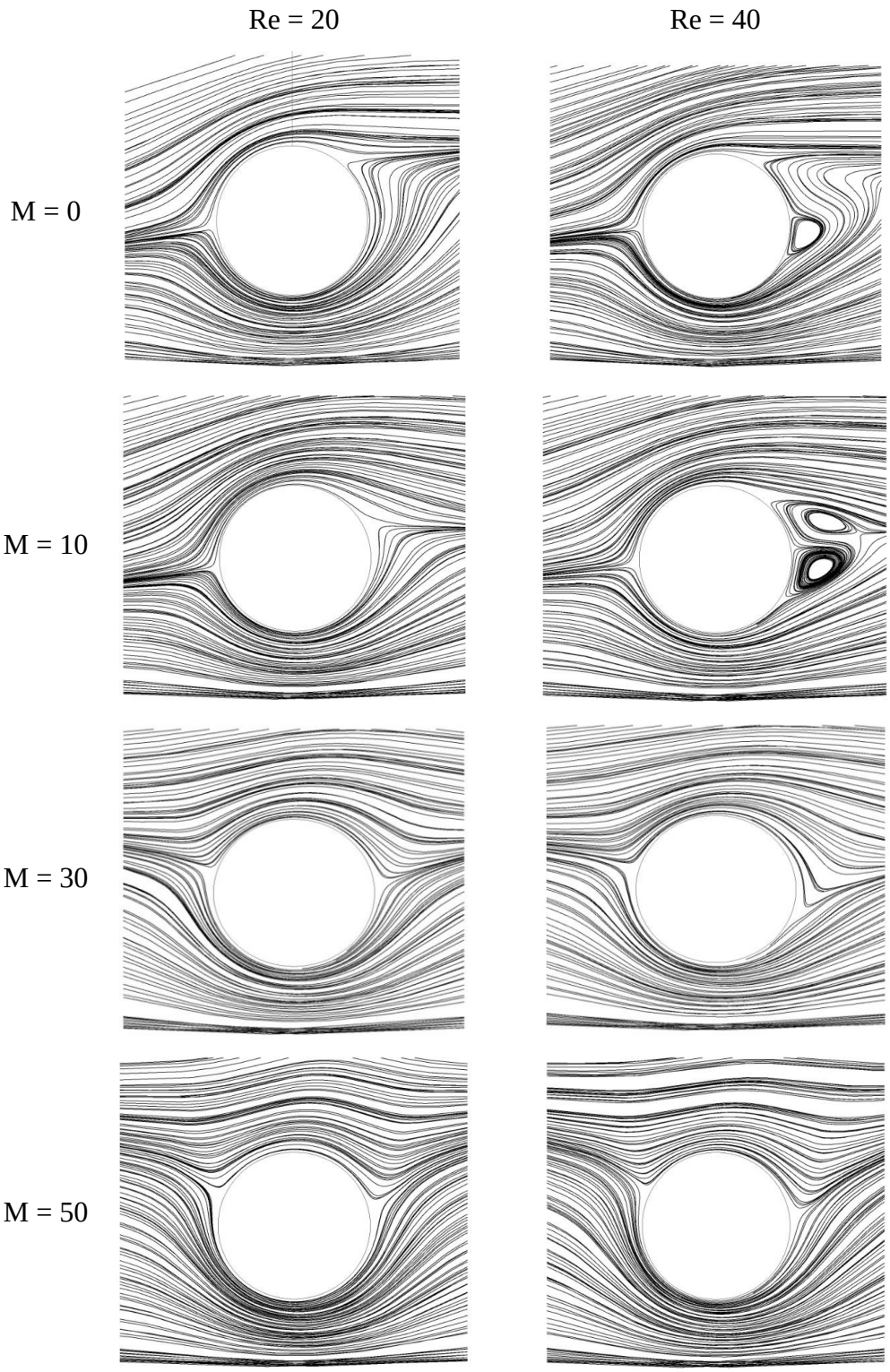

Fig. 3. Velocity streamlines around the cylinder for the radial-poloidal plane at $z = 0$. Left images show the results for $\mathrm{Re} = 20$, right for $\mathrm{Re} = 40$. Magnetic field inclination $\alpha = 16°$

International Communications in Heat and Mass Transfer 91 (2018): 165-175. DOI: 10.1016/j.icheatmasstransfer.2017.12.010

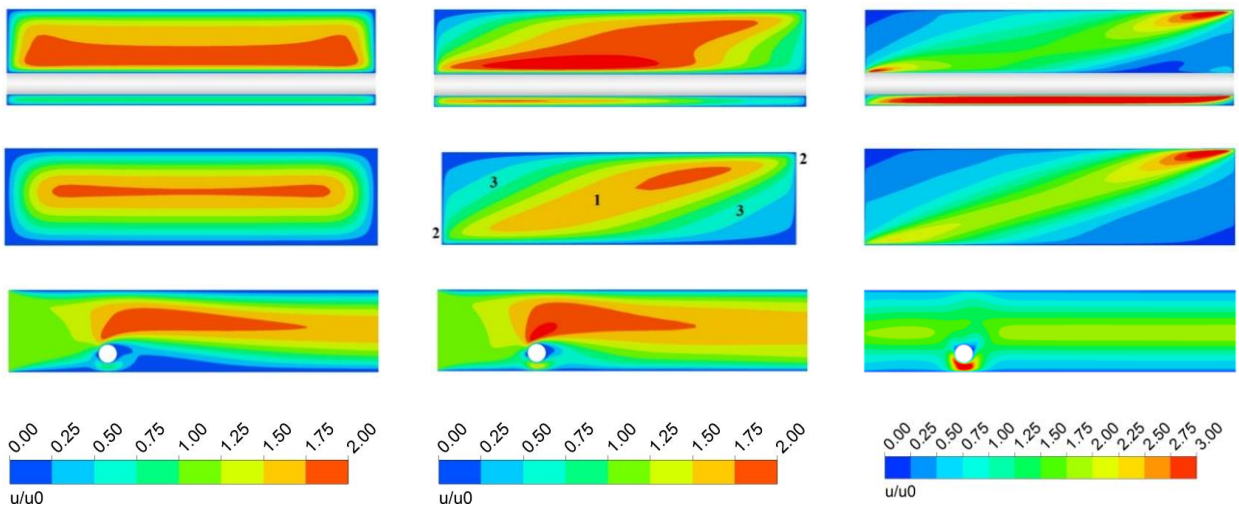

a) $M = 0$ b) $M = 10$ c) $M = 50$

Fig. 4. Velocity contour comparison for $M = 0, 10, 50$ at $Re = 20$. Top row: toroidal-poloidal view at cylinder centre ($x/d = 0$); middle row: toroidal-poloidal view at $x/d = 10$; bottom row: radial-poloidal view at $z/L = 0$. Numbers in middle row refers to 1) internal layer, 2) Hartmann boundary layer, 3) free shear layer. Note that the velocity scale for column c) covers a different range

In Table 5, the mass flow rate $\dot{m}$ calculated at $x/d = 0$ in the sub-channels, which are identified above ($y > 0$) and below ($y < 0$) the cylinder, is shown. For $M > 0$, flow rate in the bottom sub-channel increases steadily with M, reaching up to 5 times the amount found for the hydrodynamic case. The electromagnetic coupling between the two sub-channels causes this phenomenon. Since the lateral walls are conductive and are in common between the sub-channels (see Fig. 1), an induced current generated in the top can close its path through the walls of the bottom one. Therefore, the sub-channels are coupled and their flow rate tends to equalize: this phenomenon is known as Madarame effect [5]. The electric potential profile in the duct is asymmetric with a higher positive peak localized close to the top-wall. The presence of the obstacle perturbs the profile, as shown in Fig. 5a and 5b. In Fig. 6a and 6b, current streamlines for the fully developed flow and the area surrounding the cylinder are available. For the fully developed state, the currents are confined to the cross-section (i.e. toroidal-poloidal) and for this reason it is labelled as a 2D flow. Since the condition $c \gg M^{-1}$ is valid for the duct, the current paths close through the walls and avoid the boundary layers. Close to the obstacle the flow is far from the fully developed state and a gradient of velocity exists between front and rear part of the cylinder. This generates an electric potential difference, which in turn creates currents with a non-null component in the stream wise direction (see Fig. 6b). These axial currents cause an additional pressure drop term, called three-dimensional, which adds to the electromagnetic drag

International Communications in Heat and Mass Transfer 91 (2018): 165-175. DOI: 10.1016/j.icheatmasstransfer.2017.12.010

characteristic of the planar currents [5]. An overview of the 3D pressure drop incidence on the total is available in Table 4. A useful insight on this behaviour can be deduced by Fig. 7a and 7b.

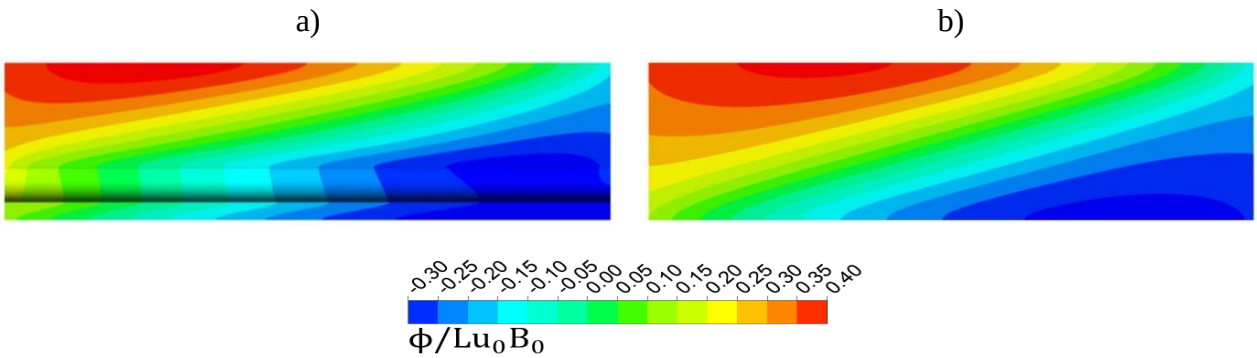

Fig. 5. Electric potential contour at $M = 10$ and $Re = 20$ for the toroidal-poloidal cross-section at a) $x/d = 0$ and b) $x/d = 10$

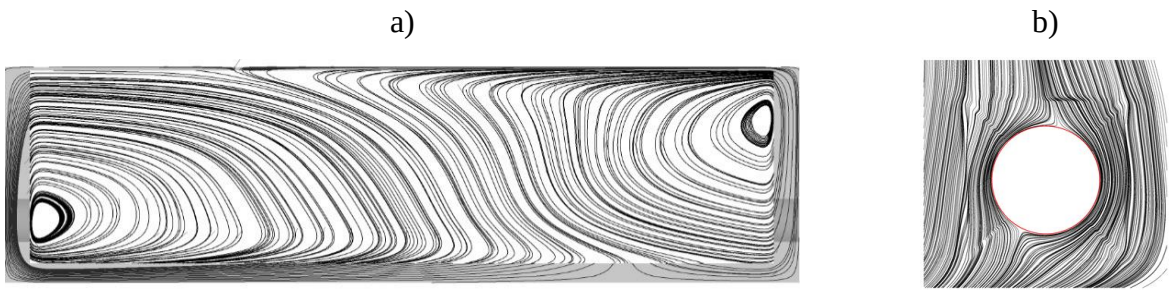

Fig. 6. Current streamlines at $M = 10$ and $Re = 20$. a) Fully developed flow at $x/d = 10$, toroidal-poloidal cross-section; b) detail of the obstacle at $z = 0$, radial-poloidal cross-section. The grey shade identifies the duct walls, the red line the cylinder surface

Since the duct walls are conductive, the pressure gradient in the channel due to the planar currents can be expressed as

$$\left.\frac{dp}{dx}\right|_{2D} \sim \frac{\sigma_w u_0 B^2 \delta_w}{L} \tag{17}$$

No simple expression can be formulated for the 3D term, since the flow geometry strongly affects it. For low intensity of the magnetic field, the pressure gradient due to the 2D flow is relatively small and, therefore, the 3D term governs the channel pressure drop. When M increases the 2D pressure gradient rises and the influence of the axial currents on the flow features is reduced. This is understandable because according to Eq. (17) it is proportional to B^2, whereas the latter have in general a weaker dependence on the induction intensity [5]. The 3D term weight decreases with the intensity of the magnetic field, falling from ~18% to ~10% for $Re = 20$ in the range considered for

this study. Enhancing the fluid mean velocity partially reverts this trend, as it is possible to see observing the $M = 30$ plots in Fig. 7b. It should be noted that this behaviour is typical of MHD flows in electroconductive channels ($c \gg M^{-1}$). For an insulating duct, the 3D term would be dominant, whereas for highly conductive walls ($c \gg 1$) the pressure gradient from the planar currents is so intense that the 3D contribute is negligible [32].

The inclination of the magnetic field plays an important role in the definition of the flow features and, consequently, the channel pressure profile. For a case with walls of non-uniform conductivity (Hunt flow), Alty [33] found that an increasing inclination of the magnetic field causes the detachment of the jets from the side walls and, for the limiting case of $\alpha = 45°$, the coalescence in a single, diagonal jet in the core region. This same phenomenon is observed in the present work. In Fig. 8 the velocity contours for various inclinations of the applied field are shown. For a purely toroidal field (Fig. 8a), the reduced electromagnetic drag in the area close to the thin wall at $y/H = +1$ causes the formation of a single jet that occupies most of the cross-section and coalesces with the suppressed one at the opposing thicker wall. Increasing the inclination, the internal layer previously described is first formed and then separates in two layers that gradually moves toward the left and right walls at $z/L = \pm 1$. For $\alpha = 90°$ (non-simulated), the magnetic field is only poloidal and the classic M-shaped flow is recovered with the formation of jets close to these walls.

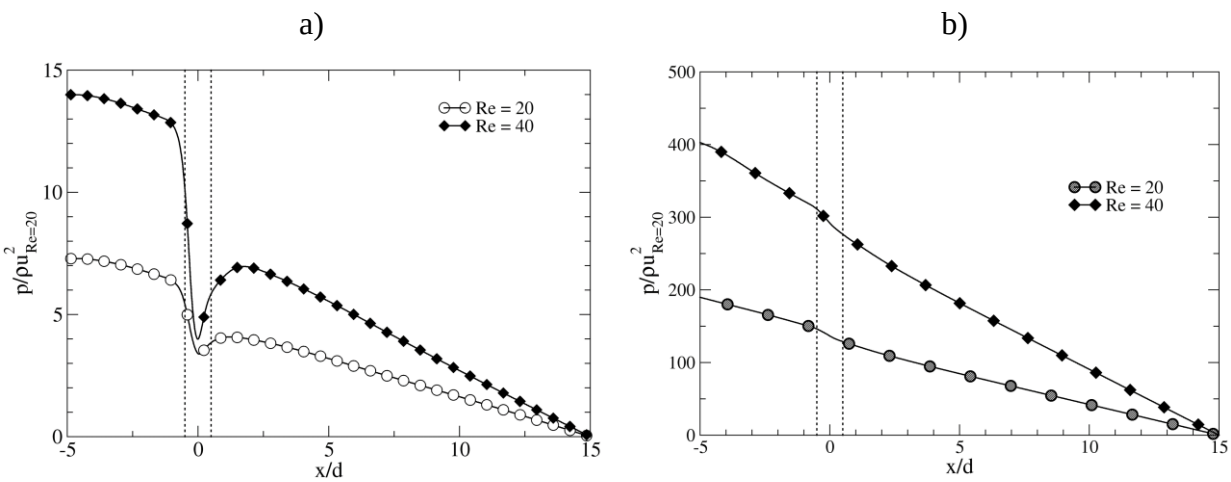

Fig. 7. Normalized pressure profile in the duct: a) plots for $M = 10$ and b) for $M = 50$. The dotted lines mark the region occupied by the cylinder

Numerical results by Kirillov et al. [9] and Hua and Walker [32] have shown that varying the inclination of the magnetic field is accompanied by a general increase of the pressure gradient. The existence of a non-monotonic behaviour was also highlighted. Although the magnetic field inclination

International Communications in Heat and Mass Transfer 91 (2018): 165-175. DOI: 10.1016/j.icheatmasstransfer.2017.12.010

considered in this work was limited to $\alpha \leq 32°$, the results obtained are in overall agreement with the literature. An overview of the behaviour of the channel pressure drop and fully developed flow pressure gradient is available in Fig. 9. The variation compared with the pressure drop for $\alpha = 16°$ is included in the range $0.9 \leq \frac{\Delta p(\alpha)}{\Delta p(16°)} \leq 1.25$.

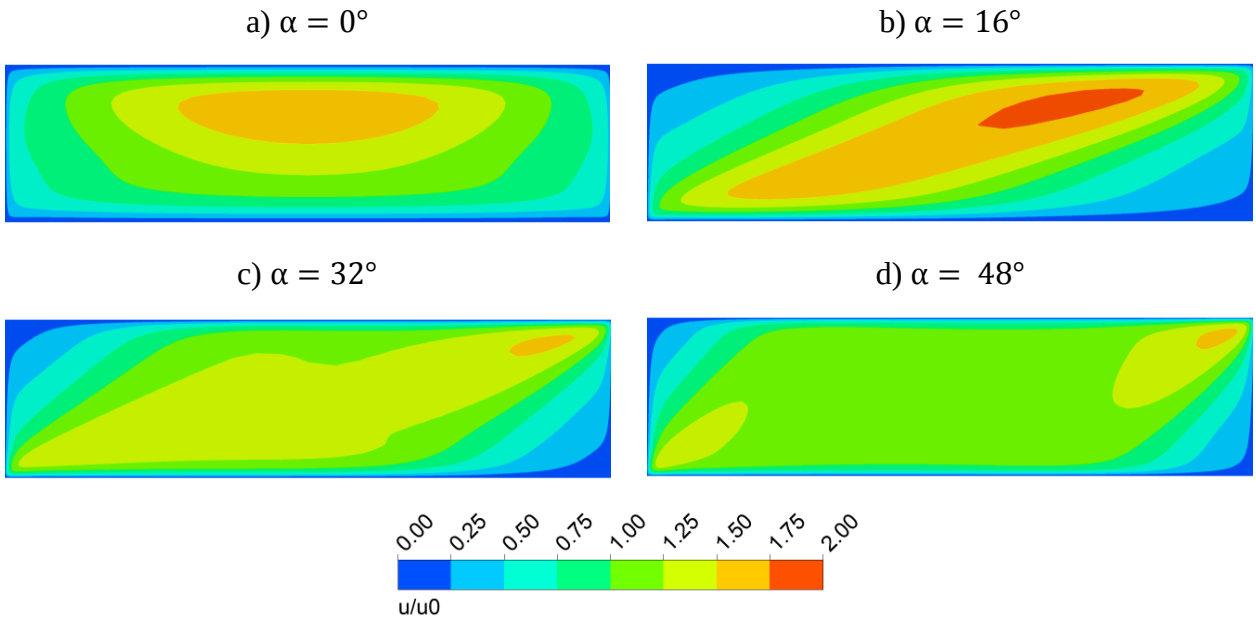

Fig. 8. Fully developed flow velocity contours for various inclinations of the magnetic field at $M = 10$ and $Re = 20$

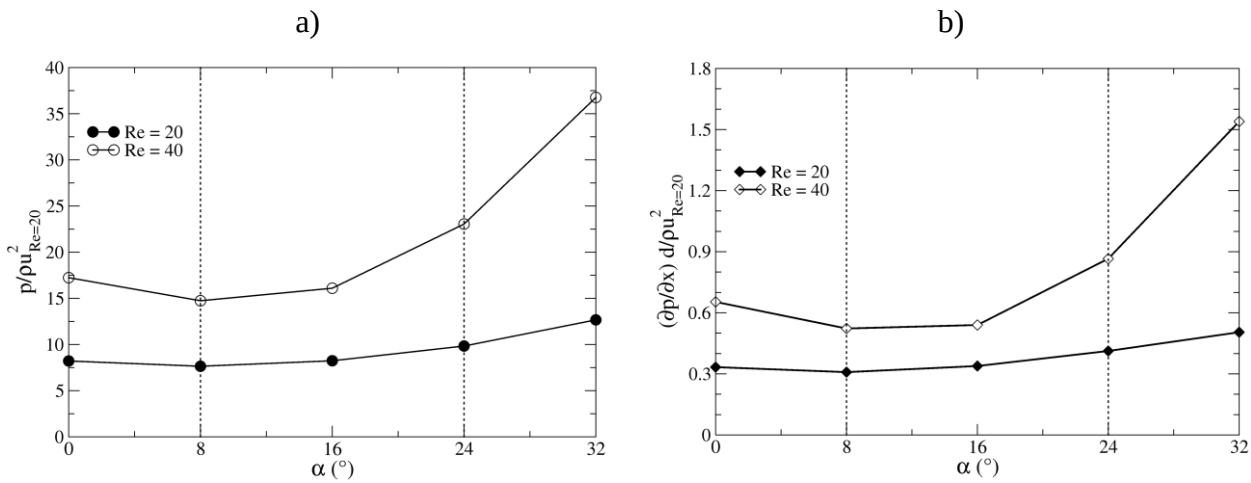

Fig. 9. Influence of magnetic field inclination for $M = 10$ on a) channel pressure drop and b) fully developed flow pressure gradient. The dotted lines identify the range of magnetic field inclination for an operative blanket [27]

International Communications in Heat and Mass Transfer 91 (2018): 165-175. DOI: 10.1016/j.icheatmasstransfer.2017.12.010

4.2 *Heat transfer*

Since the Joule heating is negligible, no additional source of power is present within the flow except the cylinder surface. Therefore, the magnetic field can enact its influence on the heat transfer mechanisms just by modifying the flow pattern. In Fig. 10, dimensionless temperature contours at $\mathrm{Re} = 20$ are presented. Since $\mathrm{Pe} = 0.68$, the advection transport is just slightly higher than the conduction, which is demonstrated by the shape of the isotherms upstream from the cylinder. Downstream, the isotherms are shifted gradually streamwise and toward the duct centreline with M, due to the stabilizing effect of the magnetic field on the flow imbalance between the top and bottom sub-channels (see Table 4).

In particular, the fluid in the latter reaches velocity much higher compared with the flow observed in the hydrodynamic case (see Fig. 4). This phenomenon increases the power removed by the flow in the cylinder bottom half and, since the peak velocity is proportional to M, the local Nusselt number is found to rise steadily along the surface. To a lesser degree, the insulating cylinder promotes the fluid velocity also in the top sub-channel. These phenomena of course affect the heat transfer.

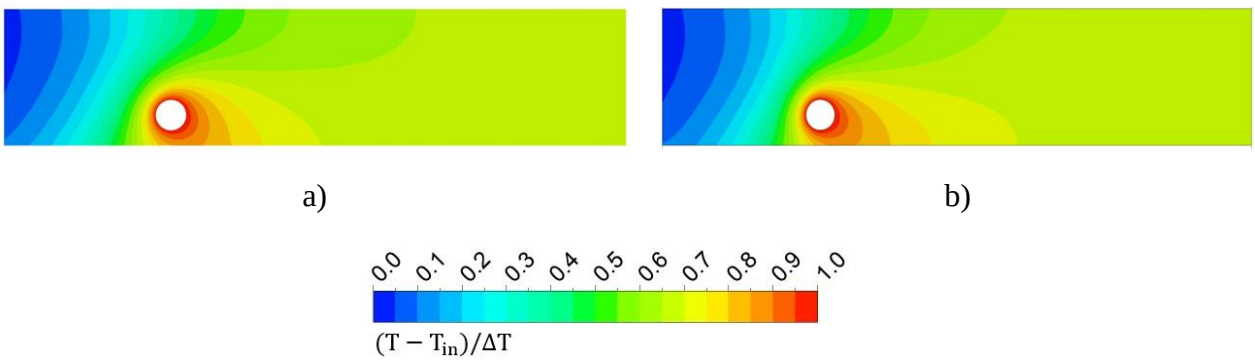

Fig. 10. Dimensionless temperature contours for the radial-poloidal cross-section at the centre of the duct for $\mathrm{Re} = 20$ a) $\mathrm{M} = 10$ and b) $\mathrm{M} = 30$

No variation was found for the average Nusselt number calculated on the obstacle surface between the reference case and the $\mathrm{M} = 10$ one. This result agrees with Chatterjee and Chatterjee [30], which for a similar simulation setup found a constant value for the flow of a liquid metal ($\mathrm{Pr} = 10^{-2}$) in the range $\mathrm{M} = [0, 10]$. However, for fluids characterized by higher Prandtl numbers Chatterjee established that the initial plateau was followed by a regime where the Nusselt numer increased with the intensity of the magnetic field. Indeed, the simulations for $\mathrm{M} > 10$ carried over by the present work show that this behaviour extends to liquid metals, as it is possible to see in Fig. 11. An higher Nu is found for $\mathrm{Re} = 40$ due to the increase in the efficiency of the convective transport mechanism for the enhanced fluid velocity. An explanation for this increment can be found in the enhancement

of the local fluid velocity around the cylinder due to the insulating surface and the improvement of the power extraction in the bottom sub-channel. Since the two plots converge at $M = 50$ for $Nu \sim 2.95$, it seems unlikely that this trend could be maintained for higher M: the mean flow suppression should eventually compensate the positive contribution to the heat transfer due to the increased flow rate in the bottom sub-channel. Further investigations are needed to assess if this trend can be expected also for a conductive cylinder surface.

The influence of the magnetic field inclination on Nu is more complex, as shown in Fig. 11b. For $\alpha = 0°$, the magnetic field is purely toroidal and, due to the low local conductivity, the flow is mostly centred in a jet close to the top wall. Alongside the wall, the side layer shows a velocity parabolic profile, which connects the peak with the Hartmann layers. When α increases, the side layer detaches from the wall and most of the flow is carried over by the internal layer. This condition is more favourable for the heat transfer since the average velocity of the fluid hitting the obstacle increases. An increment of ~6% was found for the average Nusselt number between the purely toroidal case and $\alpha = 32°$.

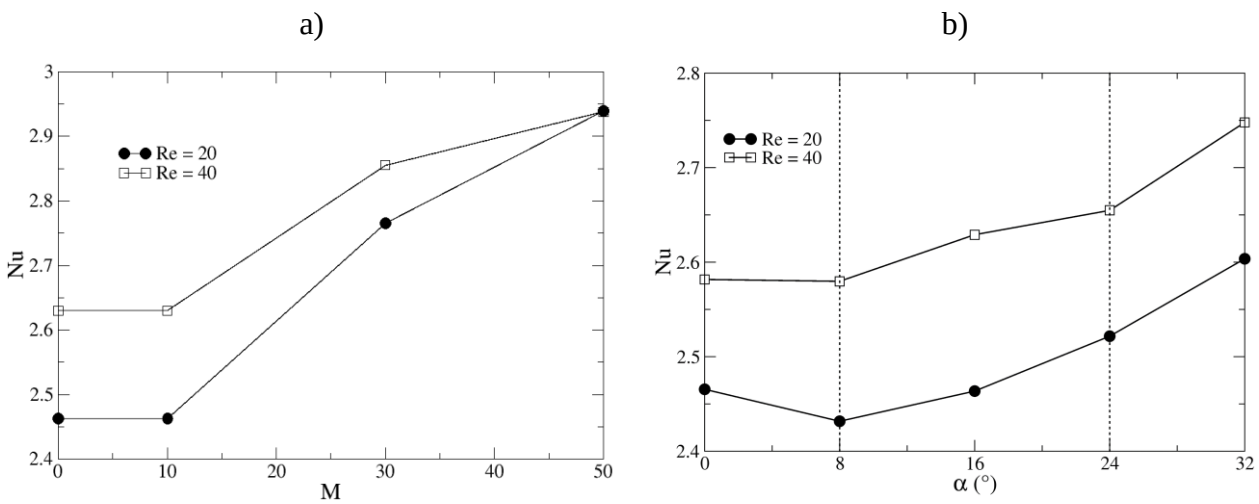

Fig. 11. Average Nusselt number on the cylinder surface; a) dependence on the Hartmann number (M) at $\alpha = 16°$and b) magnetic field inclination (α) for $M = 10$. The dotted lines identify the range of magnetic field inclination for an operative blanket [27]

The local Nusselt number (Nu_w) was plotted along the circumference of the cylinder at the centre of the duct. The results are presented in Fig. 12. The sharp increase for $\pi/2 \leq \theta \leq \pi$ can be explained as the combined result of the shifting toward the top of the cylinder of the front stagnation point and of the higher flow rate in the bottom sub-channel, which is evident comparing these plots with the velocity streamlines available in Fig. 3. Moreover, the suppression of the wake for $Re = 40$ causes the drop of local Nusselt number for the rear stagnation point ($\theta = 3\pi/2$) at $M = 50$.

International Communications in Heat and Mass Transfer 91 (2018): 165-175. DOI: 10.1016/j.icheatmasstransfer.2017.12.010

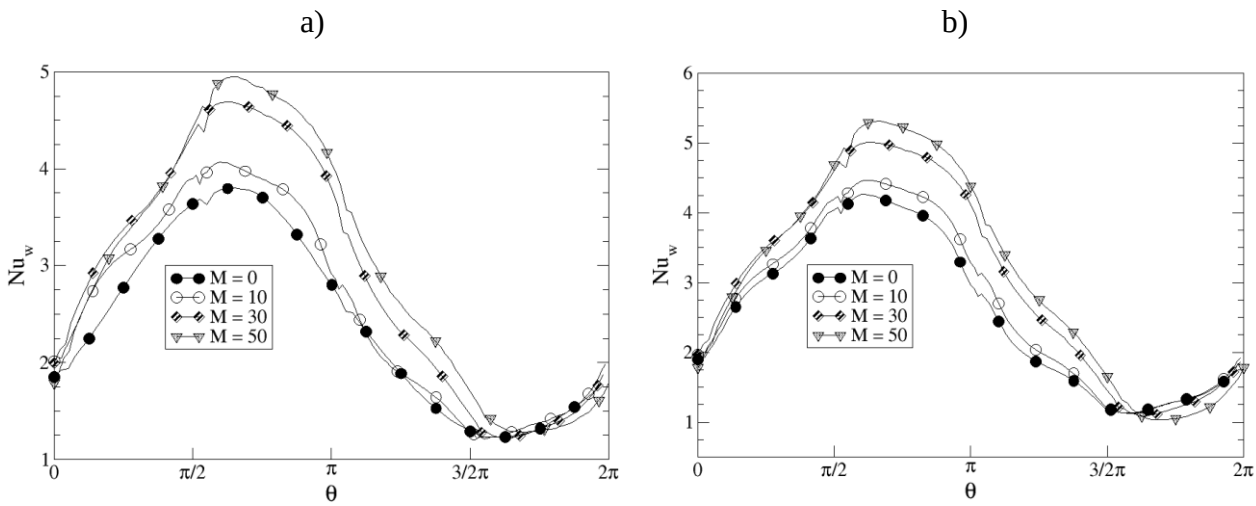

Fig. 12. Local Nusselt number on the cylinder circumference at $z = 0$; a) plot for $Re = 20$ and b) for $Re = 40$

Finally, the local Nusselt number was plotted alongside the toroidal direction for four relevant azimuthal (θ) coordinates at $Re = 20$ in Fig. 13. It is interesting to note how the Nu_w peak for the cylinder front is shifted from the centreline, following the velocity peak, whereas the highest heat transfer for the back part is verified in the hydrodynamic case due to the wake presence. Conversely, the Nu_w in the bottom part of the cylinder increases steadily with M due to the enhanced flow rate. In Fig. 12a and 12b, it is evident also the strong action of the magnetic field that strongly suppress the flow close to the walls at $z/L = \pm 1$, where the Nu_w is lower than the hydrodynamic case.

International Communications in Heat and Mass Transfer 91 (2018): 165-175. DOI: 10.1016/j.icheatmasstransfer.2017.12.010

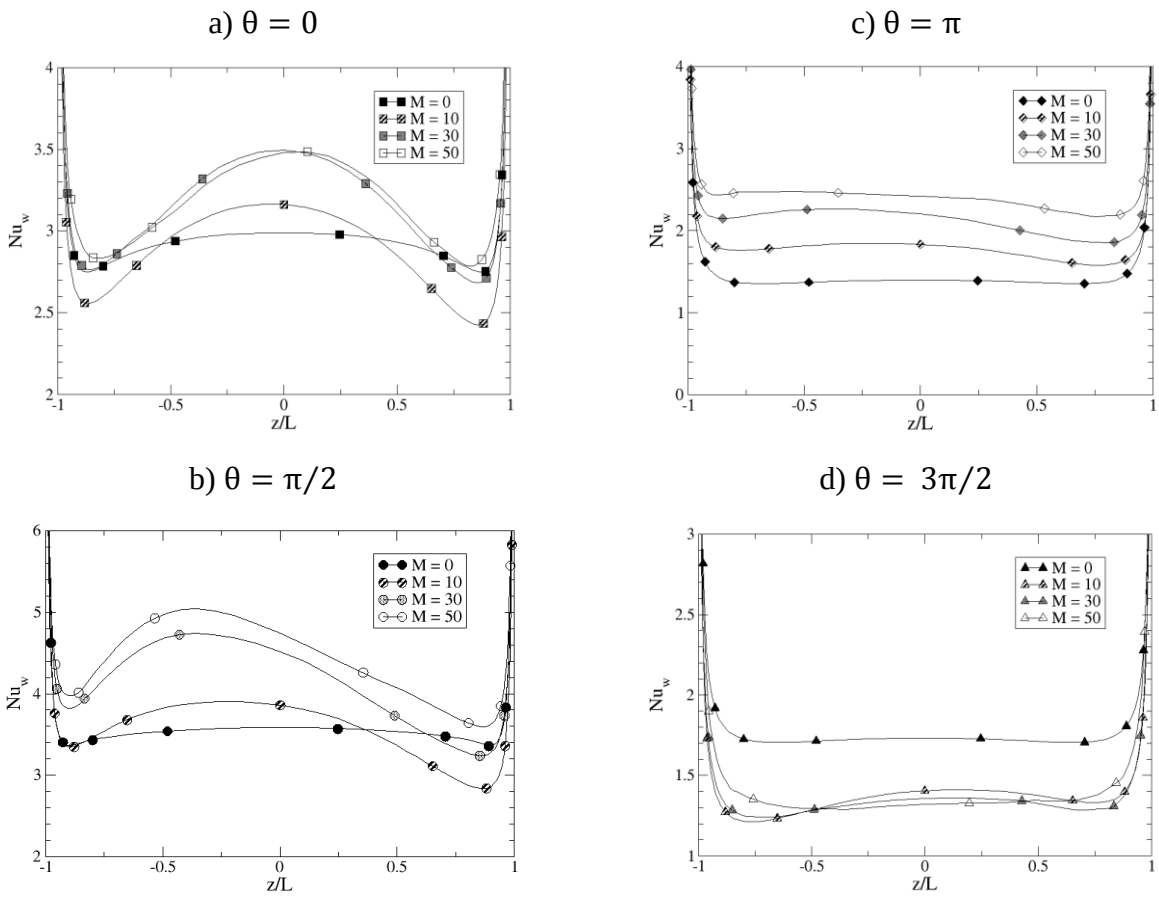

Fig. 13. Local Nusselt number on the obstacle surface at the cylinder: a) top, b) front, c) bottom and d) back point

5. CONCLUSIONS

In the present study, the MHD flow of a liquid metal past an electrically insulated circular cylinder and bounded by walls of non-uniform conductivity was investigated. The applied magnetic field was transversal to the flow and coaxial with the obstacle, featuring non-null components in both the toroidal and poloidal direction. Moreover, the cylinder was displaced by the duct centreline toward the bottom wall and its surface was kept at a fixed temperature, so that a ΔT was present between the obstacle and the fluid at the inlet.

The flow features and heat transfer for this case were investigated for low Reynolds number ($Re = 20, 40$), Hartmann number $0 \leq M \leq 50$ and magnetic field inclination relative to the toroidal axis $0° \leq \alpha \leq 32°$. The main results outlined were:

- The mass flow rate carried by the sub-channel below the obstacle increases linearly with the magnetic field intensity. For $M = 50$, an increment between 3 and 5 times compared with the hydrodynamic reference case was found. This phenomenon is caused by the electromagnetic

coupling (Madarame effect) of the sub-channels, which share the lateral conductive duct walls.

- The pressure drop in the channel can be modelled as the fully developed term (Δp_{2D}), following the scaling law for MHD flows in rectangular ducts with electroconductive walls ($\propto B^2$), plus an additional term due to the obstacle presence (Δp_{3D}) with a weaker dependence on magnetic field intensity. Thus for $M \to \infty$ and low Reynolds number flows, the pressure penalty due to the obstacle transverse to the streamwise direction becomes negligible compared with the fully developed term.
- The magnetic field inclination α influences the flow features and, in turn, the pressure gradient. A non-monotonic behaviour was found for the latter, with a local minimum for $\alpha = 8°$, and a steady increase for $\alpha \geq 16°$, which are in overall agreement with similar results available in the literature. In the range considered for the tokamak operation ($8° \leq \alpha \leq 24°$), it was found a pressure drop deviation with respect to the design inclination ($\alpha = 16°$) equal to $0.9 \leq \frac{\Delta p(\alpha)}{\Delta p(16°)} \leq 1.25$.
- Due to the enhanced mass flow rate with the magnetic field intensity, the average Nusselt number is found to increase with the Hartmann number ($\simeq 20\%$ for $M = 50$). It is unclear if this trend would be maintained for stronger magnetic fields, but it is probable that the mean flow velocity suppression will eventually overcome the positive contribution to the heat transfer from the bottom sub-channel. A reduction in the increase rate of the Nusselt number between $M = 30$ and $M = 50$ can be already observed in Fig. 11.
- The field inclination α influence on the heat transfer is found to be limited. The average Nusselt number is found to slightly increase with the inclination. In the range considered for the tokamak operation ($8° \leq \alpha \leq 24°$), the deviation with respect to the design inclination ($\alpha = 16°$) is found to be $\pm 2\%$.

Further study is required to investigate the phenomena presented in this paper for a magnetic field intensity closer to the operative fusion reactor blanket value $M = O(10^3)$. Among the topics neglected by the present study, the influence of the obstacle conductivity and buoyancy forces on the flow features are considered the most important to be addressed.

Conversely to the obstacle modelled in the present study, the cooling pipe in the blanket is electrically conductive and in direct contact with the molten metal. By providing an additional path for the closure of induced currents, the obstacle conductivity could affect the Lorentz force distribution on the cross-section which, in turn, will modify the local flow structure and heat transfer mechanisms. A follow-

up activity has been planned to investigate this phenomenon considering both an ideal perfectly conducting ($c_o = \infty$) cylinder and a "realistic" obstacle, composed of Eurofer [10].

A significative temperature gradient is expected between a fusion reactor blanket first wall and the back-supporting structure ($Gr \simeq 10^9 - 10^{12}$) which will modify the flow velocity field, causing the onset of a mixed convection regime. Hydrodynamic simulations have shown the potential for relevant heat transfer improvement compared with the forced convection case. However, these results must still be confirmed by accompanying MHD analyses [12].

REFERENCES

[1] P.A. Davidson, Magnetohydrodynamics in materials processing, Annu. Rev. Fluid Mech. 31 (1999) 273–300. doi:10.1007/978-94-007-2645-1_3.

[2] M. Abdou, N.B. Morley, S. Smolentsev, A. Ying, S. Malang, A. Rowcliffe, M. Ulrickson, Blanket/first wall challenges and required R&D on the pathway to DEMO, Fusion Eng. Des. 100 (2015) 2–43. doi:10.1016/j.fusengdes.2015.07.021.

[3] F. Dobran, Fusion energy conversion in magnetically confined plasma reactors, Prog. Nucl. Energy. 60 (2012) 89–116. doi:10.1016/j.pnucene.2012.05.008.

[4] U. Muller, L. Buhler, Magnetofluiddynamics in channels and containers, 2013.

[5] S. Smolentsev, R. Moreau, L. Bühler, C. Mistrangelo, MHD thermofluid issues of liquid-metal blankets: Phenomena and advances, Fusion Eng. Des. 85 (2010) 1196–1205. doi:10.1016/j.fusengdes.2010.02.038.

[6] R. Moreau, Y. Bréchet, L. Maniguet, Eurofer corrosion by the flow of the eutectic alloy Pb-Li in the presence of a strong magnetic field, Fusion Eng. Des. 86 (2011) 106–120. doi:10.1016/j.fusengdes.2010.08.050.

[7] P.A. Davidson, Magnetic damping of jets and vortices, J. Fluid Mech. 299 (1995) 153–186. doi:10.1017/S0022112095003466.

[8] E.M. De Les Valls, L. Batet, V. De Medina, J. Fradera, L. Sedano, Modelling of integrated effect of volumetric heating and magnetic field on tritium transport in a U-bend flow as applied to HCLL blanket concept, Fusion Eng. Des. 86 (2011) 341–356. doi:10.1016/j.fusengdes.2011.02.075.

[9] I.R. Kirillov, C.B. Reed, L. Barleon, K. Miyazaki, Present understanding of MHD and heat transfer phenomena for liquid metal blankets, Fusion Eng. Des. 27 (1995) 553–569. doi:10.1016/0920-3796(95)90171-X.

[10] P.A. Di Maio, P. Arena, G. Bongiovì, P. Chiovaro, A. Del Nevo, R. Forte, Optimization of the breeder zone cooling tubes of the DEMO Water-Cooled Lithium Lead breeding blanket,

Fusion Eng. Des. 109–111 (2016) 227–231. doi:10.1016/j.fusengdes.2016.03.021.

[11] A. Del Nevo, E. Martelli, P. Agostini, P. Arena, G. Bongiovì, G. Caruso, G. Di Gironimo, P.A. Di Maio, M. Eboli, R. Giammusso, F. Giannetti, A. Giovinazzi, G. Mariano, F. Moro, R. Mozzillo, A. Tassone, D. Rozzia, A. Tarallo, M. Tarantino, M. Utili, R. Villari, WCLL breeding blanket design and integration for DEMO 2015: status and perspectives, Fusion Eng. Des. (2017). doi:10.1016/j.fusengdes.2017.03.020.

[12] E. Martelli, A. Del Nevo, P. Arena, G. Bongiovì, G. Caruso, P.A. Di Maio, M. Eboli, G. Mariano, R. Marinari, F. Moro, R. Mozzillo, F. Giannetti, G. Di Gironimo, A. Tarallo, A. Tassone, R. Villari, Advancements in DEMO WCLL breeding blanket design and integration, Int. J. Energy Res. (2017). doi:10.1002/er.3750.

[13] M. Frank, L. Barleon, U. Müller, Visual analysis of two-dimensional magnetohydrodynamics, Phys. Fluids. 13 (2001) 2287–2295. doi:10.1063/1.1383785.

[14] V. Dousset, A. Pothérat, Numerical simulations of a cylinder wake under a strong axial magnetic field, Phys. Fluids. 20 (2008) 17104. doi:10.1063/1.2831153.

[15] W.K. Hussam, M.C. Thompson, G.J. Sheard, Dynamics and heat transfer in a quasi-two-dimensional MHD flow past a circular cylinder in a duct at high Hartmann number, Int. J. Heat Mass Transf. 54 (2011) 1091–1100. doi:10.1016/j.ijheatmasstransfer.2010.11.013.

[16] W.K. Hussam, G.J. Sheard, Heat transfer in a high Hartmann number MHD duct flow with a circular cylinder placed near the heated side-wall, Int. J. Heat Mass Transf. 67 (2013) 944–954. doi:10.1016/j.ijheatmasstransfer.2013.08.081.

[17] P.A. Davidson, An Introduction to Magnetohydrodynamics, Cambridge University Press, 2001. doi:10.1119/1.1482065.

[18] J.A. Shercliff, The boundary layer on a wall nearly parallel to a magnetic field, ZAMP Zeitschrift Für Angew. Math. Und Phys. 32 (1981) 546–554. doi:10.1007/BF00947020.

[19] Ansys Inc., ANSYS CFX Solver Theory Guide, ANSYS CFX Release 15.0. (2013).

[20] C. Mistrangelo, Three-Dimensional MHD Flow in Sudden Expansions, KfK 7201, 2006. http://d-nb.info/98018066x/34/.

[21] S.H. Kim, M.H. Kim, D.W. Lee, C. Choi, Code validation and development for MHD analysis of liquid metal flow in Korean TBM, Fusion Eng. Des. 87 (2012) 951–955. doi:10.1016/j.fusengdes.2012.02.048.

[22] A. Tassone, F. Giannetti, G. Caruso, Numerical study of laminar magneto-convection in a differentially heated square duct, J. Phys. Conf. Ser. 796 (2017) 12004. doi:0.1088/1742-6596/796/1/012004.

[23] A. Tassone, G. Caruso, A. Del Nevo, I. Di Piazza, CFD simulation of the

magnetohydrodynamic flow inside the WCLL breeding blanket module, Fusion Eng. Des. (2017) 1–5. doi:10.1016/j.fusengdes.2017.05.098.

[24] K. Mergia, N. Boukos, Structural, thermal, electrical and magnetic properties of Eurofer 97 steel, J. Nucl. Mater. 373 (2008) 1–8. doi:10.1016/j.jnucmat.2007.03.267.

[25] U. Jauch, V. Karcher, B. Schulz, G. Haase, Thermophysical Properties in the System Li-Pb, KfK 4144, 1986. http://bibliothek.fzk.de/zb/kfk-berichte/KFK4144.pdf.

[26] S. Smolentsev, S. Badia, R. Bhattacharyay, L. Bühler, L. Chen, Q. Huang, H.G. Jin, D. Krasnov, D.W. Lee, E.M. De Les Valls, C. Mistrangelo, R. Munipalli, M.J. Ni, D. Pashkevich, a. Patel, G. Pulugundla, P. Satyamurthy, a. Snegirev, V. Sviridov, P. Swain, T. Zhou, O. Zikanov, An approach to verification and validation of MHD codes for fusion applications, Fusion Eng. Des. 100 (2015) 65–72. doi:10.1016/j.fusengdes.2014.04.049.

[27] M.S. Tillack, A. Ying, H. Hashizume, The Effect of Magnetic Field Alignment on Heat Transfer in Liquid Metal Blanket Channels, Proc. IEEE Thirteen. Symp. Fusion Eng. (1989) 376–379. doi:https://doi.org/10.1109/FUSION.1989.102243.

[28] Ansys Inc., CFX Solver Modelling Guide, Release 15.0, ANSYS CFX-Solver Model. Guid. (2013). http://www.ansys.com.

[29] J. Sommeria, R. Moreau, Why, how, and when, MHD turbulence becomes two-dimensional, J. Fluid Mech. 118 (1982) 507–518. doi:10.1017/S0022112082001177.

[30] D. Chatterjee, K. Chatterjee, Wall-bounded flow and heat transfer around a circular cylinder at low Reynolds and Hartmann numbers, Heat Transf. - Asian Res. 42 (2013) 133–150. doi:10.1002/htj.21025.

[31] J.C.R. Hunt, Magnetohydrodynamic flow in rectangular ducts, J. Fluid Mech. 21 (1965) 577–590. doi:https://doi.org/10.1017/S0022112065000344.

[32] T.Q. Hua, J.S. Walker, MHD flow in rectangular ducts with inclined non-uniform transverse magnetic field, Fusion Eng. Des. 27 (1995) 703–710. doi:10.1016/0920-3796(95)90186-8.

[33] C.J.N. Alty, Magnetohydrodynamic duct flow in a uniform transverse magnetic field of arbitrary orientation, J. Fluid Mech. 48 (1971) 429–461. doi:https://doi.org/10.1017/S0022112071001691.